Letter

Hydrodynamic sound shell model

Rong-Gen Cai,[1,2,4,†] Shao-Jiang Wang,[2,‡] and Zi-Yan Yuwen[2,3,*]

[1]*School of Physical Science and Technology, Ningbo University, Ningbo 315211, China*
[2]*CAS Key Laboratory of Theoretical Physics, Institute of Theoretical Physics, Chinese Academy of Sciences, Beijing 100190, China*
[3]*School of Physical Sciences, University of Chinese Academy of Sciences, Beijing 100049, China*
[4]*School of Fundamental Physics and Mathematical Sciences, Hangzhou Institute for Advanced Study, University of Chinese Academy of Sciences, Hangzhou 310024, China*

(Received 8 May 2023; accepted 26 June 2023; published 14 July 2023)

For a cosmological first-order phase transition in the early Universe, the associated stochastic gravitational wave background is usually dominated by sound waves from plasma fluid motions, which have been analytically modeled as a random superposition of freely propagating sound shells but with the force by the scalar field that produces the self-similar profile removed. In this Letter, we propose a new analytic sound shell model by focusing on the forced propagating contribution from the initial collision stage of sound shells when their self-similar profiles are still maintained by the moving bubble walls. We reproduce the causal k^3 scaling in the infrared consistent with numerical simulations, and also recover the broad dome in the power spectrum first observed in numerical simulations. The total sound waves should contain both contributions from forced collisions and free propagation of sound shells at early and late stages of the phase transition, respectively.

DOI: 10.1103/PhysRevD.108.L021502

I. INTRODUCTION

The cosmological first-order phase transition (FOPT) [1–3], if it exists, is a violent process in the early Universe, inducing large curvature perturbations [4] or even the formation of primordial black holes [5] due to the asynchronous nature of vacuum-decay progress. The associated stochastic gravitational wave backgrounds (SGWBs) [6,7] also open a new window into the early Universe that is otherwise opaque to light for us to probe the new physics [8,9] beyond the standard model of particles physics. The nonequilibrium feature also aids the realization for the baryon asymmetry [10,11] and primordial magnetic fields [12–14].

The main sources of the SGWBs from cosmological FOPTs are bubble-wall collisions [15,16] and bulk fluid motions from both sound waves [16] and magnetohydrodynamic turbulences [15,17]. Early numerical simulations [17–21] and analytical estimations [22,23] for the bubble-wall collisions have long adopted the so-called envelope approximation that dumps the wall upon collisions, which was abandoned in later numerical simulations [24–26] with thermal fluids, leading to the recognition of longitudinal acoustic waves as the dominant contribution [27] as long-standing sources until the onset of vortical turbulences estimated both analytically [28–33] and numerically [34–37].

For a vacuum phase transition without thermal fluids, the shape of the GW spectrum from bubble-wall collisions has been analytically modeled in Ref. [38] as a broken power law (k^3, k^{-1}) in the infrared (IR) and ultraviolet (UV) limits of the wave number k, respectively, by assuming thin-wall and envelope approximations, relaxing the latter of which analytically leads to the appearance of an intermediate linear growth [39] in addition to the original broken power law as (k^3, k, k^{-1}). This intermediate linear scaling is later confirmed in a semianalytical simulation from a dubbed bulk flow model [40] beyond the envelope approximation but produces rather different UV behaviors as (k, k^{-2}) and (k, k^{-3}) for ultrarelativistic and nonrelativistic walls, respectively. Relaxing the thin-wall approximation would suppress the UV power to be steeper than k^{-1} as found in the numerical simulation [41]. An additional peak seems to emerge in the UV regime close to the bubble-wall thickness and has been observed in the numerical simulation [42] with a plausible explanation as scalar field oscillations around the true vacuum after vacuum decay.

On the other hand, for a thermal phase transition with plasma fluids, the shape of the GW spectrum is more involved as the contributions from bubble-wall collisions and bulk fluid motions are all mixed together. By detaching the fluid motions from the wall motion, a recently proposed

*Corresponding author.
yuwenziyan@itp.ac.cn
†cairg@itp.ac.cn
‡schwang@itp.ac.cn

sound shell model [43] has assumed freely propagating sound shells that were initially formed as self-similar profiles by hydrodynamics around the bubble wall, and later induces the fluid velocity field as a linear random superposition of an individual disturbance from each bubble. This sound shell model reveals the spectrum shape from sound waves as (k^5, k, k^{-3}) in the IR, intermediate, and UV regimes, respectively. The IR power k^5 was later corrected as k^9 in Ref. [44] due to the causality for the divergence-free fluid velocity field [45]. However, both the numerical simulations with spectrum shape (k^3, k^{-3}) [24–26] and a general theoretical expectation [46] prefer the usual k^3 scaling at low frequencies.

In this Letter, we propose a new analytic sound shell model by considering the initial collision stage when sound shells are still driven by the uncollided envelope of bubble walls. These forced propagating sound shells naturally lead to the usual causal k^3 scaling at low frequencies consistent with numerical simulations. We sketch the main assumptions and numerical fittings below and provide the technical details in the Supplemental Material [47].

II. FIRST-ORDER PHASE TRANSITION

Depending on the underlying particle physics model with a FOPT [48,49], the nucleation rate can either exponentially increase with time or admit a local maximum value at some time [50]. For the latter case dubbed the simultaneous nucleation [41,51], the FOPT can never be ended if the maximal number density of bubbles ever nucleated is too small for percolation to be completed within one Hubble time [52,53]. Thus, the background expansion should be carefully accounted for in the case of simultaneous nucleation with general parameter choices [54]. Hence, for the sake of simplicity without considering the Hubble expansion effect, we will focus on the former case with an exponential nucleation rate (the number of nucleated bubbles per unit time and unit volume) of the form [55–58]

$$\Gamma(t) = \Gamma(t_*)e^{\beta(t-t_*)}, \tag{1}$$

where t_* is a fixed reference time usually chosen around bubble percolations, and β^{-1} is roughly the time duration of the FOPT assumed here to be shorter than the Hubble time by $\beta/H \gg 1$ so that the background Hubble expansion can be safely neglected. The strength factor α depicts the released latent heat of vacuum decay with respect to the background radiation energy density. The last parameter is the terminal wall velocity v_w assumed here to be reached long before bubble collisions [59–62]. As the SGWB from a FOPT is of more observational interest for a larger v_w, we will mainly focus on the detonation mode of bubble expansion with its supersonic terminal wall velocity larger than the Jouguet velocity [63].

III. INITIAL SOUND SHELL PROFILE

After bubble nucleations but before bubble collisions, we assume a steady expansion of spherical thin walls with a terminal velocity v_w. Since there is no characteristic scale during bubble expansion as the initial size of nucleated bubbles can be neglected, the wall expansion and associated fluid motions can be well described with spherical coordinates (t, r, θ, φ) by a single self-similar coordinate $\xi \equiv r/(t - t_n)$ tracing the fluid element at radius r to the bubble center and at time t since bubble nucleation time t_n. Without going into the second-order hydrodynamics with shear and bulk viscosity, the total energy-momentum tensor of the scalar-bubble/plasma-fluid system with a FOPT can be well approximated as a perfect fluid form [64] $\hat{T}_{\mu\nu} = (\rho + p)U_\mu U_\nu + p g_{\mu\nu}$, with ρ, p, and U^μ denoting the energy density, pressure, and 4-velocity of bulk fluid, respectively. The conservation of $\hat{T}_{\mu\nu}$ further gives rise to the fluid equation of motion, which, under an additional assumption from a bag equation of state, can be explicitly solved for the fluid velocity profile [65] given the junction conditions at the bubble wall and shock wave front, if any. The nonvanishing part of the fluid velocity profile will be referred to as the sound shell, consisting of compression and/or rarefaction waves of bulk fluids driven by the expanding bubble wall at least before the bubble collisions.

For the detonation mode of an expanding wall with v_w, the sound shell can be numerically solved as a rarefaction wave just behind the wall with the fluid velocity profile monotonically growing from zero at $\xi = c_s$ to a maximum value v_m at $\xi = v_w$. For later convenience in analytic evaluations, we will adopt an analytical approximation

$$v_i(t, \vec{x}) = v n_i \simeq \begin{cases} \frac{v_m(r - R_1(t))}{R_2(t) - R_1(t)} n_i, & R_1(t) < r < R_2(t), \\ 0, & \text{otherwise} \end{cases} \tag{2}$$

for the fluid velocity at a radial distance r to the bubble center and time elapse $t - t_n$ since the nucleation time t_n. Here, $n_i = v_i/v$ is a unit vector from the bubble center toward the point $\vec{x}$, v_m is the fluid velocity just behind the wall, and $R_1 = c_s(t - t_n)$ and $R_2 = v_w(t - t_n)$ are the innermost and outermost radii of the sound shell. This approximation can be obtained by replacing the curve between R_1 and R_2 with a straight line.

IV. INITIAL ENERGY-MOMENTUM TENSOR PROFILE

For the computation of GWs, only the anisotropic spatial part of the energy-momentum tensor matters, that is, $T_{ij} = w\gamma^2 v_i v_j$, where $w = \rho + p$ is the enthalpy and $\gamma = (1 - v^2)^{-1/2}$ is the Lorentz factor of the 3-velocity v_i. Similar to the approximated velocity profile above, we

further approximate the enthalpy profile also with a piecewise linear function as

$$\frac{w(t,r)}{w_N} \simeq \begin{cases} \frac{w_r(r-R_1(t))}{R_2(t)-R_1(t)}+1, & R_1(t)<r<R_2(t), \\ 1, & \text{otherwise} \end{cases} \quad (3)$$

with $w_r = w_m/w_N - 1$, where w_m and w_N are the enthalpies just behind the bubble wall and at null infinity $\xi = 1$, respectively. Note that as the enthalpy behind the sound shell $w(\xi < c_s)$ deviates a constant value from that far in front of the bubble wall w_N, and the contribution of the enthalpy term to the energy-momentum tensor is suppressed by the velocity as $\xi \to c_s$; hence, the ratio $w(\xi < c_s)/w_N$ can be approximated to be 1. With approximations (2) and (3), the initial energy-momentum tensor admits nonvanishing values only within the sound shell $R_1 < r < R_2$ as

$$\begin{aligned} T_{ij} &= \frac{wv^2}{1-v^2} n_i n_j \\ &= w_N \left(\frac{w_r}{v_w - c_s} \frac{r - c_s(t-t_n)}{t-t_n} + 1 \right) \\ &\quad \times \sum_{s=0}^{\infty} \left(\frac{v_m}{v_w - c_s} \frac{r - c_s(t-t_n)}{t-t_n} \right)^{2s+2} n_i n_j, \end{aligned} \quad (4)$$

where the expansion is sufficient to take the first three terms $s = 0, 1, 2$, as the maximal bulk fluid velocity v_m is of order $\mathcal{O}(10^{-1})$. The comparison of $T_{ij}n^i n^j = w\gamma^2 v^2$ between our analytic approximation and the exact numerical evaluation is shown in Fig. 1, along with which the profiles of the enthalpy and fluid velocity from the exact self-similar solution are also shown in the inset. This energy-momentum tensor will maintain its initial profile (4) until the driven walls collide with each other, after which, the part of sound shells still driven by the uncollided envelopes of walls will continue to keep its initial hydrodynamic profile, while the remaining part of the sound shells will propagate freely with damped amplitude and widened thickness as investigated in Ref. [43]. In the rest of this Letter, we will focus on the former contribution from the forced propagating sound shells that is usually overlooked in the literature.

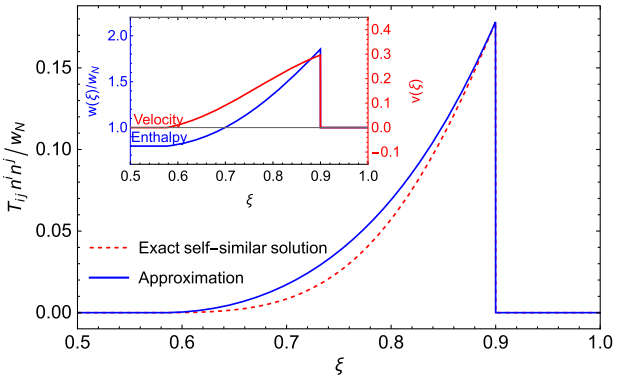

FIG. 1. The initial energy-momentum tensor profile from our approximation (4) compared to the exact numerical profile from the self-similar solution as a function of $\xi = r/(t-t_n)$ with $v_w = 0.9$, $\alpha = 0.2$. The exact numerical profiles of the fluid velocity and enthalpy are also presented in the inset.

V. SOUND SHELL FORCED COLLISIONS

Forced collisions of sound shells driven by uncollided envelopes of bubble walls will generate a GW energy-density power spectrum $P_{\rm GW}(t,k) \equiv \mathrm{d}(\rho_{\rm GW}/\rho_{\rm tot})/\mathrm{d}\ln k \equiv 2Ga_*^4/(\pi\rho_{\rm tot}a^4)\Delta(k)$ from a two-point correlation function $\langle T_{ij}(x)T_{kl}(y)\rangle$ at two space-time points x and y. Here, $\rho_{\rm GW}$ and $\rho_{\rm tot}$ are GW and critical energy densities at time t with scale factor $a(t)$, respectively, redshifted from the dimensionless spectrum $\tilde{\Delta}(k) \equiv \Delta(k)/(2\beta^{-2}w_N^2)$ at the phase-transition completion t_* with scale factor $a(t_*) \equiv a_*$. When x and y are in the same (different) sound shell, the two-point correlator $\langle T_{ij}(x)T_{kl}(y)\rangle$ serves as the single-shell (double-shell) contribution as illustrated in the schematic picture of Fig. 2. After tedious and lengthy calculations as detailed in the Supplemental Material [47], the above two contributions can be analytically expressed as formal integrals, which can be further evaluated numerically given the wall velocity v_w and strength factor α. With a typical choice for the parameters $v_w = 0.9$ and $\alpha = 0.2$, the numerical integration results for the single-shell spectrum $\tilde{\Delta}^{(s)}$ (red crosses) and double-shell spectrum $\tilde{\Delta}^{(d)}$ (blue circles) to the total GW

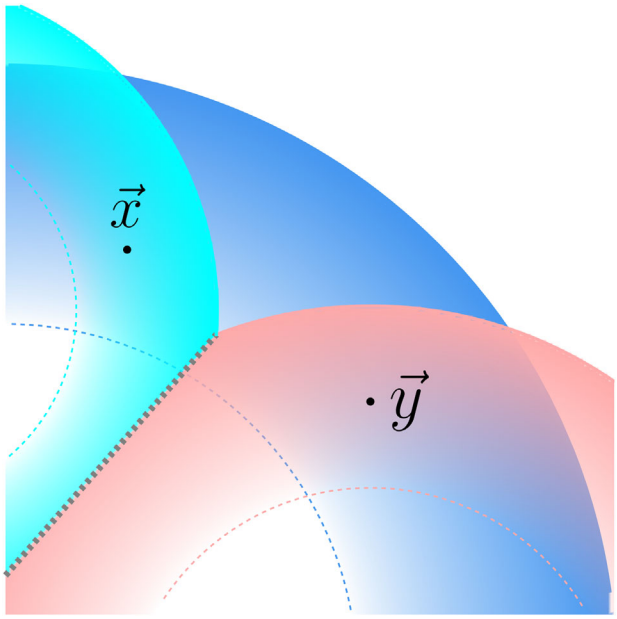

FIG. 2. A schematic illustration of the single-shell and double-shell contributions to the energy-momentum tensor with their two-point correlation functions coming from $\vec{x}$ and $\vec{y}$ in the same sound shell (blue shell) or in different sound shells (cyan and red shells).

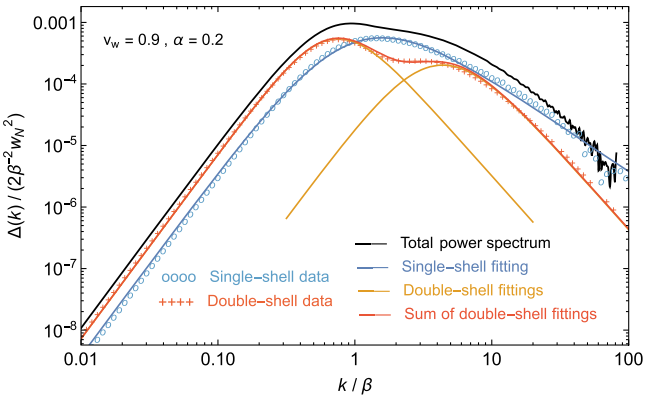

FIG. 3. The dimensionless power spectrum (black solid) from single-shell (blue circles) and double-shell (red crosses) contributions fitted by single broken-power-law (blue solid) and double broken-power-law (orange and red solid) templates, respectively, for illustrative parameters $v_w = 0.9$ and $\alpha = 0.2$.

power spectrum $\tilde{\Delta} = \tilde{\Delta}^{(s)} + \tilde{\Delta}^{(d)}$ (black solid) are shown in Fig. 3 with numerical fittings.

For practical use in extracting phase-transition parameters from numerical simulations as well as future GW observations, we provide here the fitting template from proper combinations of the broken-power-law ansatz

$$F_{n_1,n_2,\delta}(k;k_*,F_*) = F_*\left(\frac{k}{k_*}\right)^{n_1}\left(\frac{1+(k/k_*)^{\delta}}{2}\right)^{\frac{n_2-n_1}{\delta}} \quad (5)$$

depicting a peak amplitude F_* at the peak frequency k_* with a peak transition width δ^{-1} from a low-frequency slope n_1 to a high-frequency slope n_2. For our illustrative example with $\alpha = 0.2$ and $v_w = 0.9$, the single-shell power spectrum $\tilde{\Delta}^{(s)}$ is well fitted by this broken-power-law shape as

$$\tilde{\Delta}^{(s)}(k) = F_{n_1,n_2,\delta}(k;k_*,F_*) \quad (6)$$

with parameters $n_1 = 3$, $n_2 = -3/2$, $\delta = 3/2$, $k_* = \beta$, and $F_* = 4.7 \times 10^{-4}$, which asymptotes to k^3 at low frequencies and $k^{-3/2}$ at high frequencies. The double-shell power spectrum $\tilde{\Delta}^{(d)}$ admits two peaks that can be well fitted by the sum of two broken-power-law shapes as

$$\tilde{\Delta}^{(d)}(k) = F_{n_1,n_2,\delta_1}(k;k_{*1},F_{*1}) + F_{n_1,n_2,\delta_2}(k;k_{*2},F_{*2}) \quad (7)$$

with parameters $n_1 = 3$, $n_2 = -5/2$, $\delta_1 = 2$, $\delta_2 = 3/2$, $k_{*1} = 0.7\beta$, $k_{*2} = 4\beta$, $F_{*1} = 5.4 \times 10^{-4}$, and $F_{*2} = 1.0 \times 10^{-4}$, which again asymptotes to k^3 at low frequencies but $k^{-5/2}$ at high frequencies.

More general results with another fixed $\alpha = 0.1$ but varying $v_w = 0.8$–1.0 are shown in the Supplemental Material [47], from which we can learn that, for both contributions, the low-frequency behaviors always recover the causal k^3 scaling, consistent with both numerical simulations [24–26] and general analytic expectation [46]. Furthermore, the double-shell contribution always dominates over the single-shell contribution at low frequencies, while the single-shell contribution would gradually take over the high-frequency dominance for an increasing wall velocity. Therefore, we reproduce a broader dome in the total power spectrum with a decreasing detonation wall velocity as first observed in numerical simulations [24–26]. However, except for the universal k^3 scaling at low frequencies, all other parameters admit mild extra dependence on the bubble-wall velocity and phase-transition duration as summarized below.

A. Peak amplitudes

For the case attached in the Supplemental Material [47] with fixed $\alpha = 0.1$ but varying $v_w = 0.8$–1.0, the peak amplitudes of single-shell and double-shell spectra can be naively fitted as

$$\tilde{\Delta}^{(s)}_{*} = \frac{1 - 1.84v_w + 0.85v_w^2}{-4.40 + 5.50v_w - 9.96v_w^2} \times 10^{-4}, \quad (8)$$

$$\tilde{\Delta}^{(d)}_{*1} = \frac{1 - 1.89v_w + 0.90v_w^2}{-3.33 + 7.33v_w - 3.90v_w^2} \times 10^{-4}, \quad (9)$$

$$\tilde{\Delta}^{(d)}_{*2} = \frac{1 - 1.96v_w + 0.96v_w^2}{-1.58 + 2.94v_w + 1.14v_w^2} \times 10^{-4}. \quad (10)$$

The peak amplitudes for other values of the strength factor can be related to the above example with $\alpha = 0.1$ by a simple scaling relation since the pure α dependence can be factorized out approximately in a form like

$$\Delta(k, v_w, \alpha) \simeq (w_m(v_w,\alpha)v_m^2(v_w,\alpha)\gamma_m^2(v_w,\alpha))^2\hat{\Delta}(k, v_w), \quad (11)$$

where $w_m(v_w,\alpha)$ and $v_m(v_w,\alpha)$ can be analytically derived from the junction condition at the bubble wall [65]. This is because, as the maximum fluid velocity v_m is small and $w_r = w_m/w_N - 1$ is also not large, the energy-momentum profiles of different α could be approximately related by

$$\frac{T_{ij}(v_w,\alpha_1)n^i n^j}{T_{kl}(v_w,\alpha_2)n^k n^l} = \frac{w_m(v_w,\alpha_1)v_m^2(v_w,\alpha_1)\gamma_m^2(v_w,\alpha_1)}{w_m(v_w,\alpha_2)v_m^2(v_w,\alpha_2)\gamma_m^2(v_w,\alpha_2)}. \quad (12)$$

Therefore, the peak frequencies and spectrum slope are essentially encoded in $\hat{\Delta}(k, v_w)$ independent of α, while the peak amplitudes can be transformed back and forth by applying Eq. (11) as long as any one of them is known.

B. Peak frequencies

To physically fit the peak frequencies from our numerical results, we first identify two characteristic length scales. The first scale is the averaged separation of bubbles at the

onset of nucleation, which is twice the averaged bubble radius $R_w = (8\pi)^{1/3} v_w \beta^{-1} \equiv k_w^{-1}$ at collisions. The second scale is the thickness of sound shell $L_s = R_w(v_w - c_s)/v_w \equiv k_s^{-1}$. Then, the peak frequency for the single-shell spectrum can be well fitted at

$$k_*^{(s)} = 3.78 k_w, \tag{13}$$

and for the double-shell spectrum, the lower peak frequency can be well fitted at

$$k_{*1}^{(d)} = C\left(\frac{k_s}{k_w}\right)^n k_s = C\left(\frac{k_w}{k_s}\right)^m k_w \tag{14}$$

with $n = -0.74$, $m + n = -1$, and $C = 1.54$, while the higher peak frequency can be well fitted at

$$k_{*2}^{(d)} = \frac{1 - (2 - \delta_1) v_w + (1 + \delta_1) v_w^2}{\delta_2 + (0.1 + \delta_3) v_w - (0.1 - \delta_3) v_w^2}. \tag{15}$$

C. Spectrum slopes

Because of numerical errors from integrating irregular regions of sound shell collisions, spectrum slopes at high frequencies are extremely difficult to be determined precisely, especially the single-shell spectrum. For the example shown in the Supplemental Material [47], the high-frequency slopes of the single-shell spectrum vary roughly from k^{-2} to k^{-1} as v_w increases from 0.80 to 1.00, while for the double-shell spectrum, the high-frequency slopes drop from $k^{-5/2}$ to k^{-3} more confidently. These behaviors might be related to the sound shell thickness, similar to that observed previously in the numerical simulation [41] of wall collisions with varying wall thicknesses. This allows us to constrain v_w from spectrum slopes besides the usual peak frequencies and amplitudes if the SGWBs of the FOPTs are observed in the future. It might as well be that the correct UV slope be captured by the free collisions of sound shells. We leave the precise v_w dependence of spectrum slopes for future work.

D. Present spectrum

The SGWBs from FOPTs propagate as noninteracting radiations whose energy density evolves with a^{-4}. The scale factor a_* at the end of phase transition is related to that a_0 at present by [38]

$$\frac{a_*}{a_0} = 8.0 \times 10^{-16} \left(\frac{g_*}{100}\right)^{-\frac{1}{3}} \left(\frac{T_*}{100\ \mathrm{GeV}}\right)^{-1}, \tag{16}$$

where g_* is the total number of degrees of freedom of relativistic species at phase-transition temperature T_*. The peak frequency at present redshifted by a_*/a_0 reads

$$k_0 = 1.65 \times 10^{-5}\ \mathrm{Hz} \left(\frac{g_*}{100}\right)^{\frac{1}{6}} \left(\frac{T_*}{100\ \mathrm{GeV}}\right) \left(\frac{\beta}{H_*}\right) \left(\frac{k_*}{\beta}\right). \tag{17}$$

The GW power spectrum at present is redshifted as

$$\begin{aligned} \frac{\mathrm{d}\Omega_{\mathrm{GW}}}{\mathrm{d}\ln k} &= 1.67 \times 10^{-5} \left(\frac{g_*}{100}\right)^{-\frac{1}{3}} \frac{2G}{\pi \rho_{\mathrm{tot}}} (2\beta^{-2} w_N^2) \tilde{\Delta}(k) \\ &= 4.51 \times 10^{-6} \left(\frac{g_*}{100}\right)^{-\frac{1}{3}} \left(\frac{H_*}{\beta}\right)^2 \left(\frac{1}{1+\alpha}\right)^2 \tilde{\Delta}(k), \end{aligned} \tag{18}$$

where the total energy density $3H_*^2/(8\pi G) = \rho_{\mathrm{tot}} = \rho_{\mathrm{rad}} + \epsilon$ consists of the released vacuum energy $\epsilon = \alpha \rho_{\mathrm{rad}}$ and thermal radiations with the enthalpy $w_N = (4/3)\rho_{\mathrm{rad}}$. Compared to the usual GW spectrum template with the combination $[\kappa_v \alpha/(1+\alpha)]^2$ factorized out, we prefer to keep the efficiency factor κ_v [65] hidden in the dimensionless $\tilde{\Delta}$ due to the scaling relation (11).

VI. CONCLUSIONS AND DISCUSSION

The SGWBs from the bulk fluid motions, especially the sound waves, are the dominant GW sources for cosmological FOPTs provided that most bubble walls collide with each other long after they have approached the terminal velocity [61,62]. Because of the limited computational power, numerical simulations are usually implemented for a limited parameter space, making the analytic auxiliary modeling an indispensable tool to extract from the numerical simulations the fitting templates of the GW spectrum that are used for specific model predictions. The analytic auxiliary modeling [43,44] for GWs from sound waves has only considered the late-time free collisions of sound shells but overlooked the early-time forced collisions of sound shells, which has been computed analytically in the present work for the detonation mode of bulk fluid motions. We have successfully recovered the causal k^3 scaling at low frequencies and revealed the underlying structure of a widened dome around the peak frequency from a combination of single-shell and double-shell contributions, all consistent with numerical simulations. The final sound-wave spectrum (k^3, k^{-3}) suggested by numerical simulations should be a combination of the forced and free collisions of sound shells producing the k^3 scaling and k^{-3} scaling in the IR and UV regimes, respectively,

$$\left.\frac{\mathrm{d}\Omega_{\mathrm{GW}}}{\mathrm{d}\ln k}\right|_{\mathrm{SW}} = \left.\frac{\mathrm{d}\Omega_{\mathrm{GW}}}{\mathrm{d}\ln k}\right|_{\mathrm{SW}}^{\mathrm{forced}} + \left.\frac{\mathrm{d}\Omega_{\mathrm{GW}}}{\mathrm{d}\ln k}\right|_{\mathrm{SW}}^{\mathrm{free}}. \tag{19}$$

Several improvements can be made in future works for better analytic auxiliary modelings as follows.

First, for completeness, the GWs from forced collisions of sound shells should also be computed for deflagration

cases of Jouguet and weak types, the latter of which has been recently shown to be feasible for strongly coupled FOPTs [66]. All these calculations should be carried out for more realistic sound shell profiles beyond the simple linear interpolation and bag equation of state [67–71].

Second, our analytic sound waves from forced collisions of sound shells driven by the envelope of uncollided walls have neglected the contributions from the overlapping parts of colliding sound shells. This envelope approximation of sound shell forced collisions might be the reason why our high-frequency slopes from both single-shell and double-shell spectra deviate from numerical simulations.

Third, although our analytic model has achieved much better agreement with simulations than either sound shell model [43,44] or bulk flow model [39,40] by reproducing the causal IR scaling and double-peak structure, respectively, the envelope approximation we have adopted for the forced collisions of sound shells during the percolation stage, similar to the bulk flow model, also results in an extra suppression factor H_*/β in the GW spectrum compared to the sound shell model and numerical simulation results. Future analytic study of sound shell collisions both during and after bubble percolations should go beyond the envelope approximation of sound shells.

Last, the Hubble expansion effect has been considered in previous modelings of wall collisions [72] and sound waves [73], which should also be accounted for even though we expect it to be small as our forced collisions of sound shells are mainly important at the early stage of collisions when the sound shells still maintain their self-similar profiles.

ACKNOWLEDGMENTS

This work is supported by the National Key Research and Development Program of China Grants No. 2021YFC2203004, No. 2021YFA0718304, and No. 2020YFC2201502, the National Natural Science Foundation of China Grants No. 12105344, No. 12235019, No. 11821505, No. 11991052, and No. 11947302, and the Science Research Grants from the China Manned Space Project, Grant No. CMS-CSST-2021-B01. We acknowledge the use of HPC of ITP-CAS.

[1] A. Mazumdar and G. White, Review of cosmic phase transitions: Their significance and experimental signatures, Rep. Prog. Phys. **82**, 076901 (2019).
[2] M. B. Hindmarsh, M. Lüben, J. Lumma, and M. Pauly, Phase transitions in the early Universe, SciPost Phys. Lect. Notes **24**, 1 (2021).
[3] R. Caldwell *et al.*, Detection of early-Universe gravitational wave signatures and fundamental physics, Gen. Relativ. Gravit. **54**, 156 (2022).
[4] J. Liu, L. Bian, R.-G. Cai, Z.-K. Guo, and S.-J. Wang, Constraining First-Order Phase Transitions with Curvature Perturbations, Phys. Rev. Lett. **130**, 051001 (2023).
[5] J. Liu, L. Bian, R.-G. Cai, Z.-K. Guo, and S.-J. Wang, Primordial black hole production during first-order phase transitions, Phys. Rev. D **105**, L021303 (2022).
[6] C. Caprini *et al.*, Science with the space-based interferometer eLISA. II: Gravitational waves from cosmological phase transitions, J. Cosmol. Astropart. Phys. 04 (2016) 001.
[7] C. Caprini *et al.*, Detecting gravitational waves from cosmological phase transitions with LISA: An update, J. Cosmol. Astropart. Phys. 03 (2020) 024.
[8] R.-G. Cai, Z. Cao, Z.-K. Guo, S.-J. Wang, and T. Yang, The gravitational-wave physics, Natl. Sci. Rev. **4**, 687 (2017).
[9] L. Bian *et al.*, The gravitational-wave physics II: Progress, Sci. China Phys. Mech. Astron. **64**, 120401 (2021).
[10] A. G. Cohen, D. B. Kaplan, and A. E. Nelson, Progress in electroweak baryogenesis, Annu. Rev. Nucl. Part. Sci. **43**, 27 (1993).
[11] D. E. Morrissey and M. J. Ramsey-Musolf, Electroweak baryogenesis, New J. Phys. **14**, 125003 (2012).
[12] T. Vachaspati, Magnetic fields from cosmological phase transitions, Phys. Lett. B **265**, 258 (1991).
[13] Y. Di, J. Wang, R. Zhou, L. Bian, R.-G. Cai, and J. Liu, Magnetic Field and Gravitational Waves from the First-Order Phase Transition, Phys. Rev. Lett. **126**, 251102 (2021).
[14] J. Yang and L. Bian, Magnetic field generation from bubble collisions during first-order phase transition, Phys. Rev. D **106**, 023510 (2022).
[15] E. Witten, Cosmic separation of phases, Phys. Rev. D **30**, 272 (1984).
[16] C. J. Hogan, Gravitational radiation from cosmological phase transitions, Mon. Not. R. Astron. Soc. **218**, 629 (1986).
[17] M. Kamionkowski, A. Kosowsky, and M. S. Turner, Gravitational radiation from first order phase transitions, Phys. Rev. D **49**, 2837 (1994).
[18] A. Kosowsky, M. S. Turner, and R. Watkins, Gravitational radiation from colliding vacuum bubbles, Phys. Rev. D **45**, 4514 (1992).
[19] A. Kosowsky, M. S. Turner, and R. Watkins, Gravitational Waves from First Order Cosmological Phase Transitions, Phys. Rev. Lett. **69**, 2026 (1992).
[20] A. Kosowsky and M. S. Turner, Gravitational radiation from colliding vacuum bubbles: Envelope approximation to many bubble collisions, Phys. Rev. D **47**, 4372 (1993).

[21] S. J. Huber and T. Konstandin, Gravitational wave production by collisions: More bubbles, J. Cosmol. Astropart. Phys. 09 (2008) 022.
[22] C. Caprini, R. Durrer, and G. Servant, Gravitational wave generation from bubble collisions in first-order phase transitions: An analytic approach, Phys. Rev. D **77**, 124015 (2008).
[23] C. Caprini, R. Durrer, T. Konstandin, and G. Servant, General properties of the gravitational wave spectrum from phase transitions, Phys. Rev. D **79**, 083519 (2009).
[24] M. Hindmarsh, S. J. Huber, K. Rummukainen, and D. J. Weir, Gravitational Waves from the Sound of a First Order Phase Transition, Phys. Rev. Lett. **112**, 041301 (2014).
[25] M. Hindmarsh, S. J. Huber, K. Rummukainen, and D. J. Weir, Numerical simulations of acoustically generated gravitational waves at a first order phase transition, Phys. Rev. D **92**, 123009 (2015).
[26] M. Hindmarsh, S. J. Huber, K. Rummukainen, and D. J. Weir, Shape of the acoustic gravitational wave power spectrum from a first order phase transition, Phys. Rev. D **96**, 103520 (2017); **101**, 089902(E) (2020).
[27] D. J. Weir, Revisiting the envelope approximation: Gravitational waves from bubble collisions, Phys. Rev. D **93**, 124037 (2016).
[28] A. Kosowsky, A. Mack, and T. Kahniashvili, Gravitational radiation from cosmological turbulence, Phys. Rev. D **66**, 024030 (2002).
[29] A. D. Dolgov, D. Grasso, and A. Nicolis, Relic backgrounds of gravitational waves from cosmic turbulence, Phys. Rev. D **66**, 103505 (2002).
[30] A. Nicolis, Relic gravitational waves from colliding bubbles and cosmic turbulence, Classical Quantum Gravity **21**, L27 (2004).
[31] C. Caprini and R. Durrer, Gravitational waves from stochastic relativistic sources: Primordial turbulence and magnetic fields, Phys. Rev. D **74**, 063521 (2006).
[32] G. Gogoberidze, T. Kahniashvili, and A. Kosowsky, The spectrum of gravitational radiation from primordial turbulence, Phys. Rev. D **76**, 083002 (2007).
[33] C. Caprini, R. Durrer, and G. Servant, The stochastic gravitational wave background from turbulence and magnetic fields generated by a first-order phase transition, J. Cosmol. Astropart. Phys. 12 (2009) 024.
[34] P. Niksa, M. Schlederer, and G. Sigl, Gravitational waves produced by compressible MHD turbulence from cosmological phase transitions, Classical Quantum Gravity **35**, 144001 (2018).
[35] A. Roper Pol, S. Mandal, A. Brandenburg, T. Kahniashvili, and A. Kosowsky, Numerical simulations of gravitational waves from early-Universe turbulence, Phys. Rev. D **102**, 083512 (2020).
[36] A. Brandenburg, E. Clarke, Y. He, and T. Kahniashvili, Can we observe the QCD phase transition-generated gravitational waves through pulsar timing arrays?, Phys. Rev. D **104**, 043513 (2021).
[37] A. Brandenburg, G. Gogoberidze, T. Kahniashvili, S. Mandal, A. Roper Pol, and N. Shenoy, The scalar, vector, and tensor modes in gravitational wave turbulence simulations, Classical Quantum Gravity **38**, 145002 (2021).
[38] R. Jinno and M. Takimoto, Gravitational waves from bubble collisions: An analytic derivation, Phys. Rev. D **95**, 024009 (2017).
[39] R. Jinno and M. Takimoto, Gravitational waves from bubble dynamics: Beyond the envelope, J. Cosmol. Astropart. Phys. 01 (2019) 060.
[40] T. Konstandin, Gravitational radiation from a bulk flow model, J. Cosmol. Astropart. Phys. 03 (2018) 047.
[41] D. Cutting, E. G. Escartin, M. Hindmarsh, and D. J. Weir, Gravitational waves from vacuum first order phase transitions II: From thin to thick walls, Phys. Rev. D **103**, 023531 (2021).
[42] D. Cutting, M. Hindmarsh, and D. J. Weir, Gravitational waves from vacuum first-order phase transitions: From the envelope to the lattice, Phys. Rev. D **97**, 123513 (2018).
[43] M. Hindmarsh, Sound Shell Model for Acoustic Gravitational Wave Production at a First-Order Phase Transition in the Early Universe, Phys. Rev. Lett. **120**, 071301 (2018).
[44] M. Hindmarsh and M. Hijazi, Gravitational waves from first order cosmological phase transitions in the sound shell model, J. Cosmol. Astropart. Phys. 12 (2019) 062.
[45] R. Durrer and C. Caprini, Primordial magnetic fields and causality, J. Cosmol. Astropart. Phys. 11 (2003) 010.
[46] R.-G. Cai, S. Pi, and M. Sasaki, Universal infrared scaling of gravitational wave background spectra, Phys. Rev. D **102**, 083528 (2020).
[47] See Supplemental Material at http://link.aps.org/supplemental/10.1103/PhysRevD.108.L021502 for the analytical derivations on the single-shell and double-shell contributions to the total GW energy-density power spectrum from the forced collisions of sound shells.
[48] A. Kobakhidze, C. Lagger, A. Manning, and J. Yue, Gravitational waves from a supercooled electroweak phase transition and their detection with pulsar timing arrays, Eur. Phys. J. C **77**, 570 (2017).
[49] R.-G. Cai, M. Sasaki, and S.-J. Wang, The gravitational waves from the first-order phase transition with a dimension-six operator, J. Cosmol. Astropart. Phys. 08 (2017) 004.
[50] R. Jinno, S. Lee, H. Seong, and M. Takimoto, Gravitational waves from first-order phase transitions: Towards model separation by bubble nucleation rate, J. Cosmol. Astropart. Phys. 11 (2017) 050.
[51] D. Cutting, M. Hindmarsh, and D. J. Weir, Vorticity, Kinetic Energy, and Suppressed Gravitational Wave Production in Strong First Order Phase Transitions, Phys. Rev. Lett. **125**, 021302 (2020).
[52] A. H. Guth and E. J. Weinberg, Could the Universe have recovered from a slow first order phase transition?, Nucl. Phys. **B212**, 321 (1983).
[53] M. S. Turner, E. J. Weinberg, and L. M. Widrow, Bubble nucleation in first order inflation and other cosmological phase transitions, Phys. Rev. D **46**, 2384 (1992).
[54] J. Ellis, M. Lewicki, and J. M. No, On the maximal strength of a first-order electroweak phase transition and its gravitational wave signal, J. Cosmol. Astropart. Phys. 04 (2019) 003.
[55] S. R. Coleman, The fate of the false vacuum. 1. Semiclassical theory, Phys. Rev. D **15**, 2929 (1977); **16**, 1248(E) (1977).

[56] C. G. Callan, Jr. and S. R. Coleman, The fate of the false vacuum. 2. First quantum corrections, Phys. Rev. D **16**, 1762 (1977).
[57] A. D. Linde, Fate of the false vacuum at finite temperature: Theory and applications, Phys. Lett. **100B**, 37 (1981).
[58] A. D. Linde, Decay of the false vacuum at finite temperature, Nucl. Phys. **B216**, 421 (1983); **B223**, 544(E) (1983).
[59] J. Ellis, M. Lewicki, J. M. No, and V. Vaskonen, Gravitational wave energy budget in strongly supercooled phase transitions, J. Cosmol. Astropart. Phys. 06 (2019) 024.
[60] J. Ellis, M. Lewicki, and V. Vaskonen, Updated predictions for gravitational waves produced in a strongly supercooled phase transition, J. Cosmol. Astropart. Phys. 11 (2020) 020.
[61] R.-G. Cai and S.-J. Wang, Effective picture of bubble expansion, J. Cosmol. Astropart. Phys. 03 (2021) 096.
[62] M. Lewicki and V. Vaskonen, Gravitational waves from bubble collisions and fluid motion in strongly supercooled phase transitions, Eur. Phys. J. C **83**, 109 (2023).
[63] P. J. Steinhardt, Relativistic detonation waves and bubble growth in false vacuum decay, Phys. Rev. D **25**, 2074 (1982).
[64] S.-J. Wang and Z.-Y. Yuwen, Hydrodynamic backreaction force of cosmological bubble expansion, Phys. Rev. D **107**, 023501 (2023).
[65] J. R. Espinosa, T. Konstandin, J. M. No, and G. Servant, Energy budget of cosmological first-order phase transitions, J. Cosmol. Astropart. Phys. 06 (2010) 028.
[66] L. Li, S.-J. Wang, and Z.-Y. Yuwen, Bubble expansion at strong coupling, arXiv:2302.10042.
[67] F. Giese, T. Konstandin, K. Schmitz, and J. van de Vis, Model-independent energy budget for LISA, J. Cosmol. Astropart. Phys. 01 (2021) 072.
[68] F. Giese, T. Konstandin, and J. van de Vis, Model-independent energy budget of cosmological first-order phase transitions–A sound argument to go beyond the bag model, J. Cosmol. Astropart. Phys. 07 (2020) 057.
[69] X. Wang, F. P. Huang, and X. Zhang, Energy budget and the gravitational wave spectra beyond the bag model, Phys. Rev. D **103**, 103520 (2021).
[70] S.-J. Wang and Z.-Y. Yuwen, The energy budget of cosmological first-order phase transitions beyond the bag equation of state, J. Cosmol. Astropart. Phys. 10 (2022) 047.
[71] X. Wang, C. Tian, and F. P. Huang, Model-dependent analysis method for energy budget of the cosmological first-order phase transition, arXiv:2301.12328.
[72] H. Zhong, B. Gong, and T. Qiu, Gravitational waves from bubble collisions in FLRW spacetime, J. High Energy Phys. 02 (2022) 077.
[73] H.-K. Guo, K. Sinha, D. Vagie, and G. White, Phase transitions in an expanding universe: Stochastic gravitational waves in standard and non-standard histories, J. Cosmol. Astropart. Phys. 01 (2021) 001.